Optics Letters

Simultaneous holographic imaging and light-scattering pattern measurement of individual microparticles

MATTHEW J. BERG[1,*] AND STEPHEN HOLLER[2]

[1]Department of Physics, Kansas State University, 116 Cardwell Hall, Manhattan, Kansas 66506-2601, USA
[2]Department of Physics & Engineering Physics, Fordham University, 441 E. Fordham Road, Bronx, New York 10458, USA
*Corresponding author: matt.berg@phys.ksu.edu

Received 24 May 2016; accepted 14 June 2016; posted 23 June 2016 (Doc. ID 266910); published 15 July 2016

This work combines digital holography with spatial filtering at two wavelengths to record the hologram and light-scattering pattern for a single particle using a color sensor. Particles 30–100 μm in size and with various shapes are considered. The results demonstrate the ability to unambiguously associate a complicated scattering pattern with the particle size, shape, and orientation.

OCIS codes: (090.1995) Digital holography; (290.5850) Scattering, particles; (290.3200) Inverse scattering; (290.2558) Forward scattering.

http://dx.doi.org/10.1364/OL.41.003363

The characterization of micron-sized particles is an important need in science and engineering, and this is especially true for aerosols [1]. For example, determining the size, shape, and abundance of particles present in the atmosphere is crucial to our understanding of the radiative forcing of the atmosphere [1,2]. Other examples include the detection of biological aerosols for agricultural and public-health concerns [3]. Typically, "characterization" refers to determination of a particle's size, shape, and in some cases its material composition. Often, this must be done in a contact-free manner as the collection of particles for microscope-based characterization may distort the true morphology, e.g., consider liquid or frozen particles. This motivates the use of light scattering due to its inherent contact-free nature.

There are two elements to this light-scattering analysis. First, the one- or two-dimensional (2D) scattered intensity pattern produced by an illuminated particle is measured. This can be done very well on the single- and multi-particle level using a variety of techniques [1]. Second, the pattern must then be interpreted to infer the desired particle characteristics, and herein lies much difficulty. This is because there is no general mathematical relationship between a measured pattern and the (unknown) particle characteristics. Thus, the interpretation step must involve *a priori* information or make strong assumptions that often relate to the particle shape [1,4]. There is generally no guarantee that the particle size and shape one associates with a pattern is in fact the correct one; a limitation known as the inverse problem.

It is possible, however, to image a particle in a contact-free manner with digital holography [5–7]. Here, the interference pattern produced by the unscattered and scattered light, i.e., the hologram, is recorded by a 2D CCD sensor. Then, a Fourier transform operation is applied computationally to this digital hologram to yield a silhouette-like image of the particle; see [5,8] for explanation. In this way the particle's size, shape, and orientation may be known unambiguously provided that the image resolution of the sensor is not exceeded. The drawback is that the scattering pattern is not readily known since what is measured derives from the superposition of the unscattered and scattered light rather than the scattered light alone. Knowledge of the scattering pattern is nevertheless important as it describes how the particle redistributes light, which, e.g., is key to quantifying the radiative impacts of atmospheric aerosols [1]. The pattern also contains information about the particle's material composition, which is not directly available from the holographic image.

This Letter describes a proof-of-principle experiment where the digital hologram of a single particle is measured simultaneously with the particle's 2D light-scattering pattern around the forward direction. Following generation of the particle image, the pattern can then be unambiguously and quantitatively associated with the size, shape, and orientation of the particle producing it. Thus, in a sense, this work constitutes a laboratory-based solution to the inverse problem as it relates to size and shape determination. While there are examples of seemingly similar experiments, e.g., see [9], this work is unique in that the pattern and image are obtained from the *same* particle at the *same* time. With this capability, the validity of scattering-pattern-only characterization techniques and instrumentation could be directly assessed and their capabilities improved.

Figure 1 shows the optical layout, which begins with a CW He–Ne laser emitting at 632.8 nm and a *Q*-switched Nd:YLF laser frequency doubled to emit at 526.5 nm. These will be called red and green light, respectively. Following the red beam path first, the light passes through a linear polarizer to ensure vertical polarization, next a Pockels cell, and then a second polarizer oriented horizontally. In this way, the CW red beam can be pulsed on demand on the nanosecond scale by activating

the Pockels cell. The purpose of this polarization gating is discussed more below.

Following a spatial filter (SF1) to smooth and expand the beam, the light passes through a beam splitter cube (BSC) and on to illuminate the particle, which is deposited onto an antireflection (AR)-coated window called the "stage." The red beam is roughly 10 mm wide after SF1, so much of the light passes by the particle unscattered. Both unscattered and scattered light then encounter a dichroic optic called the "composite filter." This is designed to be transparent to red but reflective to green light. Transmitted red light is then received by a color CCD sensor (Point Grey Research Inc., GS3-U3-120S6C-C) located ~50 mm from the stage. The red beam is expanded so that the unscattered and scattered light interfere across all of the sensor chip. The two light wavelengths used are close to the transmission peaks of the sensor's pixel-level RGB color filters, resulting in minimal, but not negligible, "cross talk" between the color channels.

Now consider the green beam, which also passes through a polarizer to ensure vertical polarization and another spatial filter (SF2) to smooth, but not expand, the beam profile. Upon entering the BSC the light combines with the red beam, yet the beams do not interfere since they are cross polarized at this point. The green beam then illuminates the particle stage, where most of the light passes unscattered. Now, however, the green light does not yet reach the sensor but is reflected by the composite filter.

This filter is a combination of three separate filters: two long-pass dichroic filters with a cut-on wavelength of 567 nm sandwiching a green-light absorption filter (GAF); see Fig. 1 left inset. Thus, green light is reflected by either side of the composite filter while red light is transmitted. Since the dichroic filters are not 100% opaque to green light, some of the intense unscattered light will leak through and saturate the sensor. To prevent this, the GAF removes any green while still passing red light.

Following reflection from the composite filter, the unscattered and scattered green light are intercepted by a positive lens, L_1. The path length from the particle to L_1 is the same as the lens' focal length (50 mm), and thus, the unscattered light is focused to a waist while the scattered light is collimated. Unscattered and scattered light is shown by solid and dashed beam paths in Fig. 1, respectively. Next is a mirror with a 500 μm diameter through-hole at its center oriented at 45° to the mirror axis (Lenox Laser Inc., AL-45-500-CUST-2″). This is called the spatial-filter mirror (SFM) for short and is positioned in the back focal plane of L_1 such that unscattered light passes while scattered light is reflected. This spatial filtering allows the intense unscattered light to be separated from the much weaker scattered light [10].

The scattered light is then passed through a third spatial filter (SF3) to block any stray light that is not already removed by the SFM. This is a crucial step since ambient dust that collects on the optical surfaces preceding SF3, or that may float through the beam paths, can pollute the scattering pattern. Incidentally, this will also eliminate the need to use an air-tight cell in future work when the flowing aerosol stream is introduced, cf. [3,5]. More discussion of this is given below.

Given the diameter of the SFM through-hole and the focal length of L_1, about 0.3° of the forward-scattered light should be lost through the hole. In practice, however, more is lost due to scattering from the hole rim, which constitutes noise that must be removed by SF3.

The scattered light is reflected twice more and any stray red light is removed by a red absorption filter (RAF). A final lens L_2 images the output plane of SF3, denoted by Σ in Fig. 1, onto the sensor via reflection from the back side of the composite filter. In this way, the green channel of the sensor records only the 2D scattering pattern of the particle.

The particle is deposited on the stage for simplicity in this experiment, but this is not required. In future work, the stage will be replaced by a flowing aerosol stream as in [5], enabling a truly contact-free particle diagnostic ability. An optical crossed-beam trigger system, described in [11], will then be used to activate a pulse from the lasers, thus "freezing" a particle in flight.

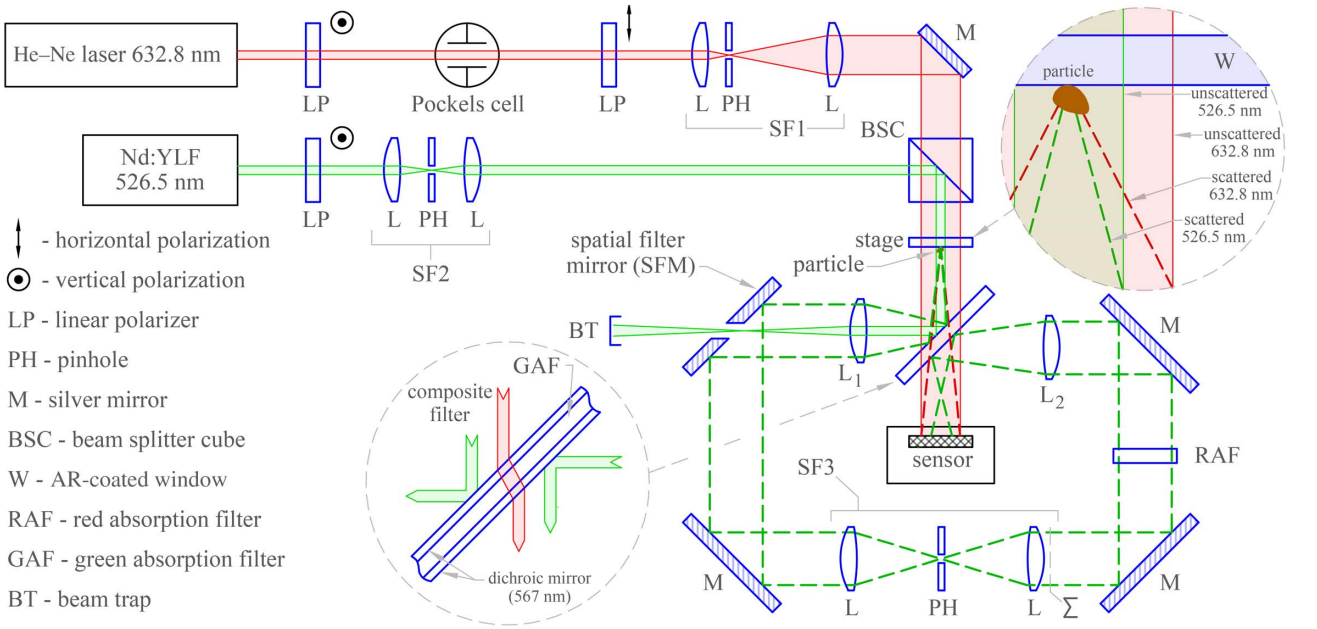

Fig. 1. Experimental arrangement to measure 2D scattering patterns simultaneous with particle images. The left inset shows details of the "composite filter" discussed in the text, and the right inset shows a particle on the "stage."

This is why the polarization gate is used on the red beam path, i.e., so that the red and green pulses can be synchronized to illuminate the particle coincidentally once sensed by the trigger.

As a first example, Fig. 2 shows the result of this measurement for a NaCl crystal aggregate on the stage. Inspection of the sensor output [Fig. 2(a)] shows the scattering pattern and hologram in green and red, respectively. Computational separation of the sensor color channels yields the pattern [Fig. 2(b)] and hologram [Fig. 2(c)] in isolation. In Fig. 2(b), the effect of the SFM hole can be seen as the dark spot at the center of the pattern. The spot is not perfectly circular due to scattering by the hole rim that is not fully removed by SF3. Moreover, the size and shape of this the spot varies slightly with the magnitude and angular width of the particle's forward-scattering lobe. Note that only a portion of the full sensor array is shown in Fig. 2 (and Fig. 4) for clarity.

By overlaying a polar-coordinate grid (θ, ϕ) on the pattern in Fig. 2(b), two scattering curves $I(\theta)$ are plotted in Fig. 2(d) in semi-log scale. These curves correspond to the $\phi = 0°$ and $\phi = 90°$ azimuthal angles indicated by red radial lines in Fig. 2(b). The sharp decline in the curves near $\theta = 0°$ is due to the SFM hole. Applying the Fourier transform operation of Eq. (2) in [12] to the hologram yields the silhouette-like particle image shown in Fig. 2(e). Note that this process involves the subtraction of a particle-free "reference" from the hologram, which is essentially a measurement of the unscattered red beam profile.

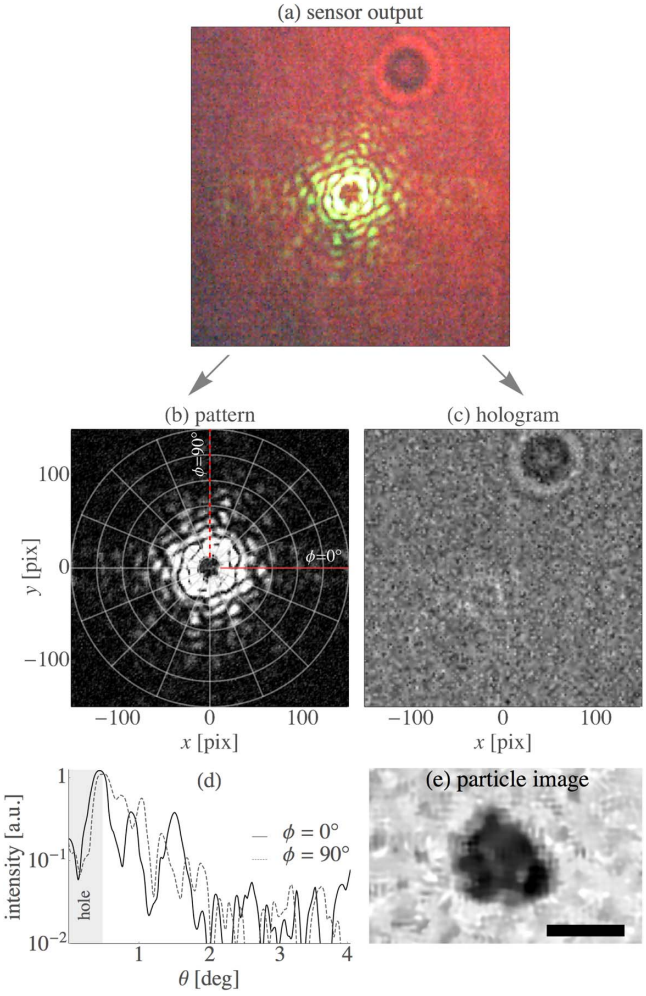

Fig. 2. Pattern measurement and holographic imaging of a NaCl crystal cluster. The scale bar in (e) is 100 μm. See text for further explanation.

Implicit here is a mapping between each pixel in the sensor to a corresponding angular coordinate, (θ, ϕ), and this is achieved through a calibration procedure. The particle stage is replaced by a precision pinhole of which two are used: 30 and 50 μm in diameter. The diffraction pattern recorded in the sensor's green channel is then compared to the theoretical Airy pattern, establishing the mapping. The Figure 3 inset shows the averaged measured and theoretical scattering curves for the 50 μm diameter pinhole; see below for a discussion of this averaging.

The drawback to this calibration is that no hologram is formed since undiffracted light is not passed to the sensor. Thus, the pinhole is not directly useful to calibrate the holographic images, i.e., to establish a mapping between the extent of the particle image in pixels and its true extent in microns. To do this, a National Institute of Standards and Technology (NIST)-traceable glass microsphere (Thermo Fisher Scientific, Inc.) is used on the stage. Yet, unlike the pinholes, there is uncertainty of the size of a microsphere since they are manufactured in a distribution with a 30 ± 1.1 μm mean particle diameter and a 7.6% coefficient of variation. To address this, the scattering pattern as given by Mie theory is fit to the measured pattern to determine the actual particle size. More precisely, because of the pattern's azimuthal symmetry, the fit is done to the pattern after it is averaged over ϕ, i.e., the fit is made to $\langle I \rangle = \langle I(\theta, \phi) \rangle_\phi$.

Figure 3 shows the outcome of this Mie-fitting procedure. The dark line is the averaged, measured curve $\langle I \rangle$, and the fit curve is shown as the dashed line where the Mie-fit particle radius is $R = 13.58$ μm, which is within one standard deviation of the size distribution mean. The fit is done qualitatively by gradually adjusting R and the refractive index m in Mie theory until it produces a curve exhibiting the same number and position of peaks seen in the measurement. Here, $m = 1.521 + 0i$, which agrees with the $1.52 + 0i$ provided by the manufacturer for 589 nm illumination. Rather than plotting the curves in terms of θ, they are plotted in log–log scale in terms of the dimensionless quantity qR, where $q = 2k \sin(\theta/2)$ is the scattering wave vector magnitude, and $k = 2\pi/\lambda$ with λ corresponding to the green light. The value for R

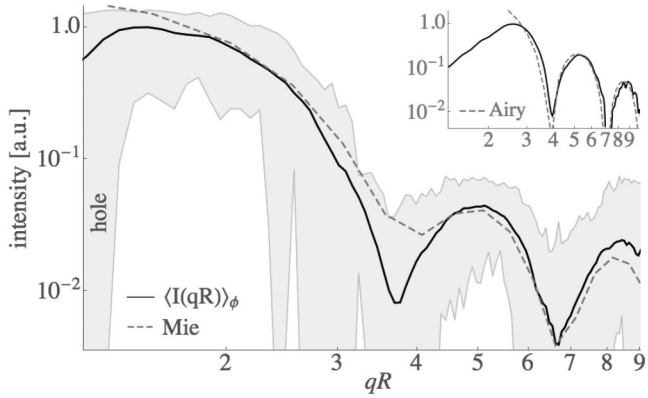

Fig. 3. Scattering-angle calibration for a 30 μm diameter microsphere and a 50 μm diameter pinhole (inset). The measured curves are normalized to their maximum intensity value, which due to the SFM hole is close to $\theta = 0$ but not exactly.

in the main plot is the sphere radius established from the Mie fit. In the inset, the known R for the pinhole is used.

A benefit of plotting $\langle I \rangle$ this way is that power law envelopes bounding the scattering curves may appear and the forward-scattering peak may be expanded enough to resolve the Guinier region, which is where the power laws crossover from an exponent of zero at $qR = 0$ to a negative value around $qR \simeq \pi/2$, e.g., see [13]. The Guinier crossover can be useful to estimate the size of a spherical particle from the scattering curve alone, although in this example the SFM hole removes too much of the forward-scattering peak to confidently locate the crossover point. The gray region in the main plot shows the range of variation of the measured curves for *specific* ϕ, where the wide range seen is due to the noisy quality of the measured pattern; cf. Fig. 4(a).

A test of the image calibration is given in Fig. 4(a) where a 50 μm diameter NIST-traceable microsphere is examined. The scattering pattern exhibits the classic nested-ring structure indicative of a spherical particle, and the inset shows the holographic particle image. As a final example, Fig. 4(b) shows the pattern and image for a pecan pollen particle. Here, a particle size of roughly 30–50 μm is seen, depending on the dimension considered, which is consistent with [14].

While the holographic images reveal the particle size, shape, and orientation, they also exhibit a degree of noise and limited resolution. The resolution is estimated to be 10–15 μm by examining a variety of NIST-traceable microspheres. Particles smaller than 10 μm could not be imaged well enough to ensure that what appeared like a single particle was not in fact a cluster. Noise in the images is likely due to stray light along the red beam, which unlike the green light could not be removed by a spatial filter. Also, the sensor's dynamic range is between 2 and 3 orders of magnitude depending on the electronic noise floor, which is much less than the range in [5] where better resolution is obtained.

A surprising conclusion from this experiment is that despite the apparent low quality of the holograms, especially in comparison to those in [5], the resulting particle images are clear enough to be useful. The resolution could be improved using a sensor with greater dynamic range, by forming the hologram with shorter wavelength light, and by employing a positive lens to magnify the hologram. Also, replacing the particle stage with a flowing aerosol stream will eliminate a large degree of stray light.

While not used in this work, the sensor's blue channel could provide useful information [15]. For example, the scattering pattern could be measured with both green and blue light. Since any changes in the patterns would be due to the change in refractive index for these wavelengths, information related to the particle's material composition may be available.

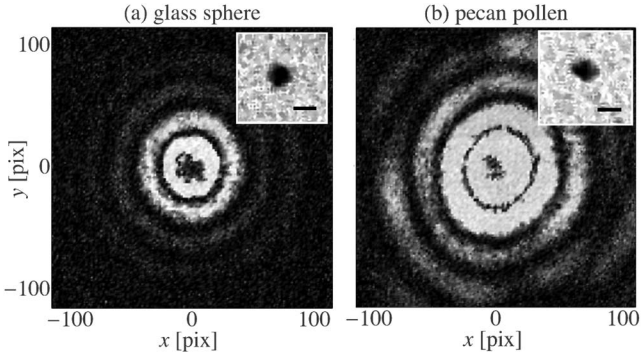

Fig. 4. Scattering pattern and particle image (insets) for (a) a 50 μm diameter glass microsphere and (b) a pecan pollen particle. The scale bar in the insets is 50 μm.

A natural question is what advantage this technique has over simply using a telemicroscope to directly image the particle via geometrical optics. In short, the answer is that the particle image can be computationally brought into focus after the fact from a *single* hologram measurement. With a telemicroscope the particle must be within the depth of field (DOF), which for flowing particles in an aerosol stream would mean some images may be strongly blurred. Also, given the micron-scale size of these particles, the DOF is also of the order of microns, and controlling the trajectory of flowing particles to this degree is challenging [3]. With the holographic technique this problem is avoided. Moreover, if multiple particles happen to be present in the stream at the instant of observation, each could be brought into focus computationally from the same measured hologram. In fact, if the holographic image resolution could be improved enough, it is possible that this computational focusing could render a three-dimensional picture of a single particle in much the same way that focusing in on a particle with a microscope gives a sense of the particle's depth; cf. [5,16].

Funding. Directorate for Geosciences (GEO); National Science Foundation (NSF) (1453987); Army Research Office (ARO) (W911NF-15-1-0549).

Acknowledgment. The authors are grateful for useful discussions with Yong-Le Pan, Kevin Aptowicz, laboratory assistance from Nava Subedi, and comments from two anonymous reviewers.

REFERENCES

1. P. Kulkarni, P. A. Baron, and K. Willeke, eds., *Aerosol Measurement: Principles, Techniques, and Applications* (Wiley, 2011).
2. U. Dusek, G. P. Frank, L. Hildebrandt, J. Curtius, J. Schneider, S. Walter, D. Chand, F. Drewnick, S. Hings, D. Jung, S. Borrmann, and M. O. Andreae, Science **312**, 1375 (2006).
3. K. B. Aptowicz, R. G. Pinnick, S. C. Hill, Y.-L. Pan, and R. K. Chang, J. Geophys. Res. **111**, D12 (2006).
4. O. Kemppinen, T. Nousiainen, S. Merikallio, and P. Räisänen, Atmos. Chem. Phys. **15**, 11117 (2015).
5. M. J. Berg and G. Videen, J. Quant. Spectrosc. Radiat. Transfer **112**, 1776 (2011).
6. J. J. Kielar, Y. Wu, S. Coëtmellec, D. Lebrun, G. Gréhan, and M. Brunel, J. Quant. Spectrosc. Radiat. Transfer **178**, 108 (2016).
7. J. J. Kielar, P. Lemaitre, C. Gobin, Y. Wu, E. Porcheron, S. Coëtmellec, G. Gréhan, and M. Brunel, Opt. Commun. **372**, 185 (2016).
8. T. Kreis, *Handbook of Holographic Interferometry: Optical and Digital Methods* (Wiley, 2005).
9. D. R. Secker, P. H. Kaye, R. S. Greenaway, E. Hirst, D. L. Bartley, and G. Videen, Appl. Opt. **39**, 5023 (2000).
10. M. J. Berg, S. C. Hill, G. Videen, and K. P. Gurton, Opt. Express **18**, 9486 (2010).
11. Y.-L. Pan, S. Holler, R. K. Chang, S. C. Hill, R. G. Pinnick, S. Niles, and J. R. Bottiger, Opt. Lett. **24**, 116 (1999).
12. M. J. Berg and N. R. Subedi, J. Quant. Spectrosc. Radiat. Transfer **150**, 36 (2015).
13. M. J. Berg, S. C. Hill, Y.-L. Pan, and G. Videen, Opt. Express **18**, 23343 (2010).
14. T. K. Haulik and L. C. Holtzhausen, J. Hortic. Sci. **63**, 567 (1988).
15. S. Holler, S. D. Fuerstenau, and C. R. Skelsey, J. Quant. Spectroc. Radiat. Transfer **178**, 167 (2016).
16. Y. Wu, X. Wu, L. Yao, M. Brunel, S. Coëtmellec, D. Lebrun, G. Gréhan, and K. Cen, Powder Technol. **295**, 96 (2016).